www.sciencemag.org/cgi/content/full/science.1199375/DC1

Supporting Online Material for

Seismic Detection of the Lunar Core

Renee C. Weber,* Pei-Ying Lin, Edward J. Garnero, Quentin Williams, Philippe Lognonne

*To whom correspondence should be addressed; E-mail: renee.c.weber@nasa.gov

Published 6 January 2011 on *Science* Express
DOI: 10.1126/science.1199375

This PDF file includes:

SOM Text
Figs. S1 to S7
Tables S1 and S2
References

Seismic detection of the lunar core

Supporting online material

Renee C. Weber,[1]* Pei-Ying Lin,[2] Edward J. Garnero,[2] Quentin Williams,[3] Philippe Lognonne[4]

[1]NASA Marshall Space Flight Center, 320 Sparkman Drive, Huntsville, AL 35805 USA
[2]Arizona State University, School of Earth and Space Exploration, Tempe, AZ
[3]U. C. Santa Cruz, Department of Earth and Planetary Sciences, Santa Cruz, CA
[4]Institut de Physique du Globe de Paris, Saint-Maur-des-Fosses, France

*To whom correspondence should be addressed; E-mail: renee.c.weber@nasa.gov.

[1] Here we provide details on the array method of stacking the lunar seismic data. Seismic signals on the Moon have long been characterized as containing a long time period (tens of minutes) of ringing following first arrivals, referred to as the seismic coda (*S1*). This has been most commonly attributed to a combination of low attenuation in the Moon and strong scattering in the megaregolith (*S2*). For some seismic arrivals, Earth signals also possess significant coda, e.g., in the crust (*S3*) as well as P-waves diffracted around Earth's core (*S4*). The background noise in the absence of quake-generated signals on Earth and the Moon may slightly differ, owing to instrumentation quality (e.g., lunar seismograms show digitization artifacts, while their terrestrial counterparts show ambient ground motion not from body waves of interest), but our array methodologies work similarly well on both bodies. In the presence of clear seismic energy (from quakes) that is well above noise levels, recordings from different stations and events can be stacked to assess signal coherency. Raw lunar seismograms were first aligned through a multi-channel cross-correlation method, then stacked for each component of motion: the vertical (Z), radial (R), and transverse (T) components. The polarization filter (*S5*) was then applied to each cluster stack. The filter (M) is a time-averaged product of the vertical and radial components of motion:

$$M_j = \sum_{i=-n}^{n} Z_{j+i} R_{j+i} \qquad (1)$$

where j is the time step, and n determines the length of the averaging window (we used n = 6 samples). The output of the filter (OZ) is the product of M and Z:

$$OZ_j = Z_j M_j \qquad (2)$$

[2] The polarization filter achieves two effects: it enhances larger amplitudes relative to smaller amplitudes (a common practice in array methods) from the triple product of seismograms, and it enhances energy that is rectilinearly partitioned onto the R and Z components of motion (while suppressing noise). Thus, an ascending PcP or P-wave, which will be present on both the Z and R components, will be enhanced compared to incoherent scattered energy. We search for P-to-P and S-to-P reflections, on the OZ traces. P-to-S reflections are vertically polarized (SV) shear waves, hence we define OR as:

$$OR_j = R_j \sum_{i=-n}^{n} Z_{j+i} R_{j+i} \qquad (3)$$

[3] For horizontally polarized shear waves (SH), energy is expected to appear solely on the transverse component of motion (T), such as the SH component of S and the core-reflection ScS. We similarly process SH data by cubing and averaging the T component:

$$OT_j = T_j \sum_{i=-n}^{n} T_{j+i} T_{j+i} \qquad (4)$$

[4] S-to-S reflections are searched for on the OT traces. In our method, we stack the polarization-filtered cluster stacks; hence we make a stack of stacks. The arrival times of core reflections are predicted from ray theory, and referenced to the hand-picked S arrival. Each trace is shifted such that the predicted arrival aligns at time t = 0, and stacked accordingly.

[5] To identify the S arrival for each cluster, we plot the raw stack components (R, T, Z) and the polarization filtered versions OZ, OR, and OT, as well as the envelopes of the polarization-filtered traces. S picks were made by considering the T, OT, and env(OT) component traces, where env() denotes the typical Hilbert-transform envelope function (*S6*). An example is shown in Fig. S1. The resulting pick is used for all components of motion on a given station from a given cluster. Since there are 106 located clusters, each with information from 4 stations, there are a total of 106 × 4 = 424 traces to evaluate for S picks. We identified 62 traces of high enough quality for reliable S picks. Some of those picks were made on different stations from the same cluster. The total number of clusters from which we made picks is 38 (Table S1). Our picks are in good agreement with those of previous studies (*S7*, *S8*). To illustrate that our conclusions are based on stack peaks that are not dominated by specific station/cluster pairs, we plot the bounce points for our 62 station/cluster pairs in Fig. S2.

[6] If a clear S arrival for a given cluster/station was not observed on any of the transverse-component traces, then we used either the vertical- or radial-component trace (whichever was strongest) if the S arrival was present and clear, noting that the radiation pattern of the S-wave might favor SV energy for some quakes, as in the case of Earth. We assigned each pick a quality factor: if the S arrival was clearly identifiable on the transverse-component traces, it was assigned a factor of 1.0. If the S arrival was less clear on the transverse-component traces, or picked on the vertical- or radial-component traces, it was assigned a factor of 0.5. Traces with no clear S arrival, or with too many strong signals in the vicinity of S, were discarded. Before stacking, we weighted individual traces by the S pick quality factor.

[7] Our choice of S as the reference arrival is due to the typically weak, ambiguous, and/or absent P arrivals. To account for potential uncertainty introduced by errors in the S compared to P results of any reference structure, as well as assuming S heterogeneity might track P heterogeneity, we tested different time windows around our predicted time of interest prior to stacking. The intent was to ensure that our reference S arrival estimate didn't miss the predicted core arrival, as well as to test the stability of our results on the time window length. Varying the

stack window length also accounts for any slight travel time differences that might arise from errors in moonquake origin time and location introduced during model extrapolation to depth. We stacked on predicted core arrival times using window lengths τ varying between 2 and 20 seconds centered on the arrival of interest.

[8] Because deep moonquake focal mechanisms are not constrained, there is no way to predict the expected polarity of core arrivals. To prevent potential opposite-polarity arrivals from negating each other in the stack, each trace was first enveloped before stacking. Taking the envelope of each trace unifies polarities in the data, allowing signals of unknown polarity to stack coherently. No additional smoothing was applied. Each trace was then normalized such that the S amplitude was equal to 1 (maximum amplitude in a 10-second window centered on the picked S arrival time). For core phases that arrive between P and S (PcP and typically ScP), if a peak higher than 1 occurred in the window between P+0.5τ and S−0.5τ, we also normalized that peak to 1 (to prevent a single trace from dominating the stack). Similarly, for phases that arrive after S (typically ScS and PcS), peaks in the window between S+0.5τ and S+500 seconds that are larger than 1 were also normalized to 1. This accommodates the possibility that the reference S wave is weak, but observable, and some deep reflection is in a favorable part of its own radiation pattern, and hence larger than direct S.

[9] Based on the predicted core radius, core phases will arrive at different times relative to the S arrival (Fig. S3). To prevent stacks on a given arrival from being modified by energy from a different arrival, we discarded traces with potentially interfering phases. When stacking for PcP, for example, if the ScP-PcP differential arrival time was smaller than 0.5τ, the trace was thrown out. Omitting traces with so-called “traffic” energy is common in terrestrial applications of array seismology aimed at deep Earth modeling.

[10] For very small core radii, core phases from shallower cluster depths will arrive at or after the time of the S arrival. In such cases, to prevent S-coda contamination, such traces were discarded. For very large core radii, deeper cluster depths will fall below the target CMB depth, where core reflections are impossible. Such traces were also discarded.

[11] The combined effects of core radius and moonquake source depths dictate the number of traces that will be stacked at each core radius value. To account for this effect when estimating the amount of energy in each stack, we normalized the area under the curve by the number of traces stacked at each depth increment.

[12] We tested the array stacking procedure on a simple model in which a single interface exists – that of the CMB for a liquid core – and searched for the P-wave reflected from this boundary (PcP). The P and S velocities at the base of the mantle in the model of (*S3*) were extended to the core-mantle boundary (noting that most part models of the lunar interior do not present model solutions in the deepest 500 km of the interior). A P-wave velocity of 4.2 km/s in the core was calculated from the equation of state of iron-sulfur alloys (*S9*, *S10*). Fig. S4 shows some example PcP ray paths for varying core radii, the associated velocity profiles and travel time curves, and the stack energy results plotted against core radius. In this example we also show the results of stacking the moonquake data on random PcP times (using a 10-second window), with the intent of establishing a baseline result to which the core energy peaks can be compared. This test gives

clear evidence for the presence of core energy in the Apollo data, and thus we were motivated to pursue models of the lunar interior that were compatible with results from other lines of research, including moment of inertia, lunar laser ranging, and electromagnetic induction (*S11*).

[13] We re-plotted our results for the multi-layered core (shown in Fig. 2) in Fig. S5 to show the baseline resulting from stacking on random core arrival times. In some cases, core energy peaks that we have identified in the stacks do not fall above one standard deviation of the baseline result. We have chosen to highlight some weak peaks because in other wave types the peak is significant. It is tempting to note that while the energy trace for the 10-second window may not fall above the baseline, some of the smaller time window traces do; however, such analysis is not appropriate since the random trials were completed using a 10-second window, and different window lengths will produce different baseline results. A second example is given in Fig. S6 using a 2-second window. Our results are largely unchanged when considering the 2-second window, thus we note that the choice of time window length does not affect our overall conclusions. The uncertainties we report for the radius of each layer represent a spread in values depending on wave type, and should not be interpreted as having resulted from a formal error estimate.

[14] We note that the amplitudes of the stacked peaks for the four wave types vary significantly, and stress that it is not possible to interpret the amplitudes in terms of reflectance strength of the different boundaries, i.e., the relative impedance contrasts. Two factors predominantly contribute to this challenge: 1) we have no knowledge about moonquake radiation patterns, and 2) the necessity of taking the envelope of traces in order to stack without destructive interference (due to unknown polarities of arrivals). Since different arrivals on different components (i.e., Z versus R versus T) may be larger or smaller in an unsystematic way, the stacked result will be directly affected in a likewise unpredictable way. Other factors also contribute to amplitude variability. For example, the amplitude of CMB reflections relative to ICB reflections depends on 1) the moonquake's radiation pattern (which is completely unknown at present, thus either arrival can be stronger), and 2) the impedance contrast at the CMB and ICB. On Earth, which is similar to the Moon in that the P-velocity change is a reduction going down into the core and an increase going down into the inner core, we commonly see ICB reflections, but not CMB reflections. The reflection coefficient of a CMB reflection is quite small. Thus, for the Moon, it is not unexpected to have a small CMB reflection (and hence small CMB amplitude in the P-to-P stack), and a somewhat larger-amplitude ICB reflection (and hence a bigger ICB amplitude in the P-to-P stack).

[15] In the case of the S-to-S stack, the reflection off of the top of the hypothesized partial melt boundary is larger than the core reflection. While it is difficult to constrain the reason, it is plausible that the core reflection is muted due to the propagation through the highly attenuating partial melt layer. However, the absolute amplitude of the S-to-S reflections off of the CMB is comparable to or larger than any other wave type (as expected). In our analyses we focused on the largest changes in amplitudes, and for the S-to-S stack, these were at the CMB and top of the partial melt layer. True constraints on the impedance contrasts of these layers will come from future ground-based geophysics missions on the Moon (*S12, S13*).

[16] We are confident that the signals we have recovered are not crustal conversions (*S14*),

which generate delays of ~8 seconds. Core arrivals are later. In addition, surface reflections occur at different times and different move-outs for each station, so they are not expected to stack coherently. Structure outside of our region of interest may generate coda arrivals that go into our stacks, and hence might influence our answers, e.g., cracks or other heterogeneity beneath the Apollo landing sites. However, we stack along the predicted arrival time move-outs of deep mantle reflections, which likewise do not systematically arrive at constant times behind, for example, a first arriving P-wave, since different stations are at different distances. Therefore, if the number of stations in any stack is high, arrivals due to unaccounted-for heterogeneity should not stack coherently, and are hence muted, and the deep reflections are enhanced. Furthermore, the structure beneath every Apollo site is not expected to be exactly similar, and hence such effects are also not expected to stack coherently.

[17] The final velocity and density structure with depth is given in Table S2. We note that small perturbations in velocities generally do not affect our results beyond minor degradation in peak coherence. For example, in Fig. S7 we show the stacked energy versus core radius for a model with v_p decreased to 8.3 km/s in the layer above the PMB.

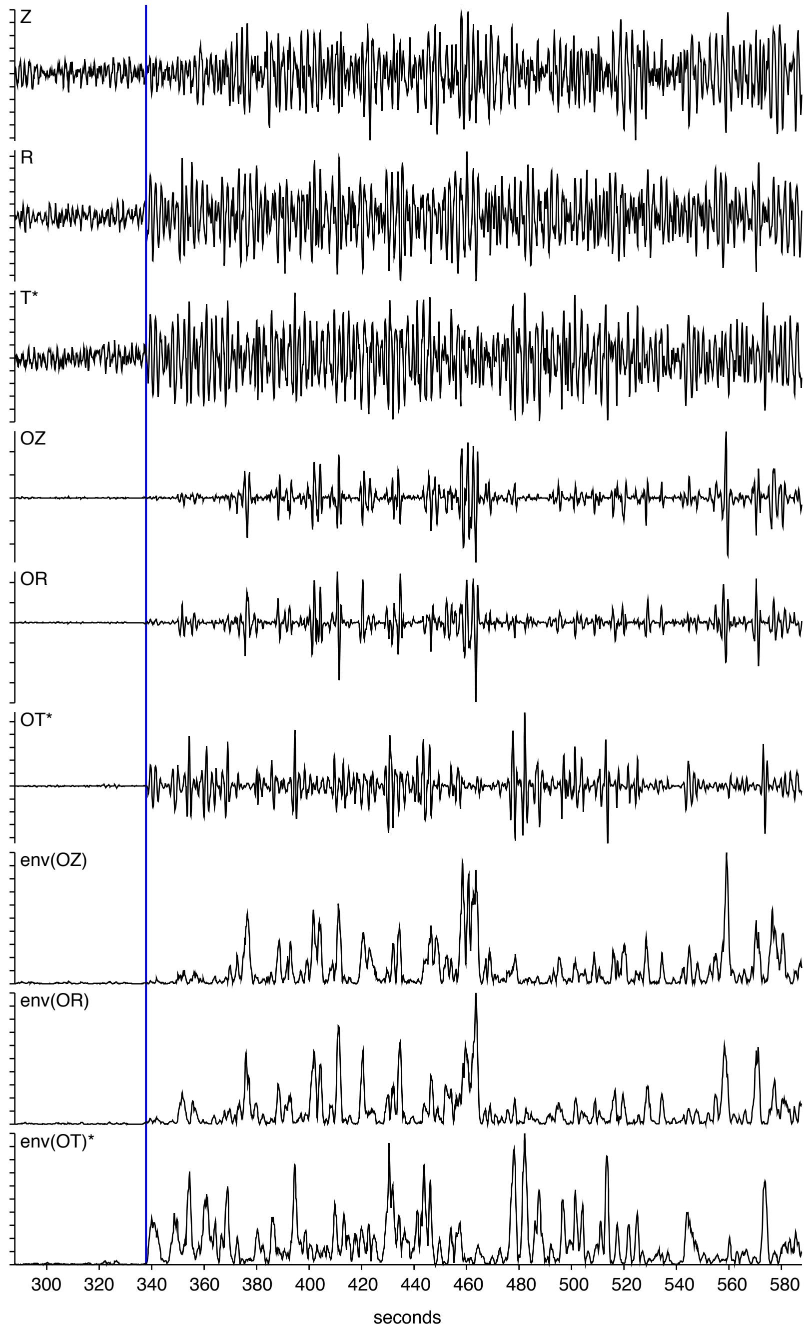

Figure S1: (top three traces): Raw deep moonquake stack components (cluster A1) at Apollo station 15. (middle three traces): Polarization filtered components of the same stack. (bottom three traces): Envelopes of the polarization-filtered traces. The S pick (blue line) was made while considering the T, OT, and env(OT) traces (marked with asterisks).

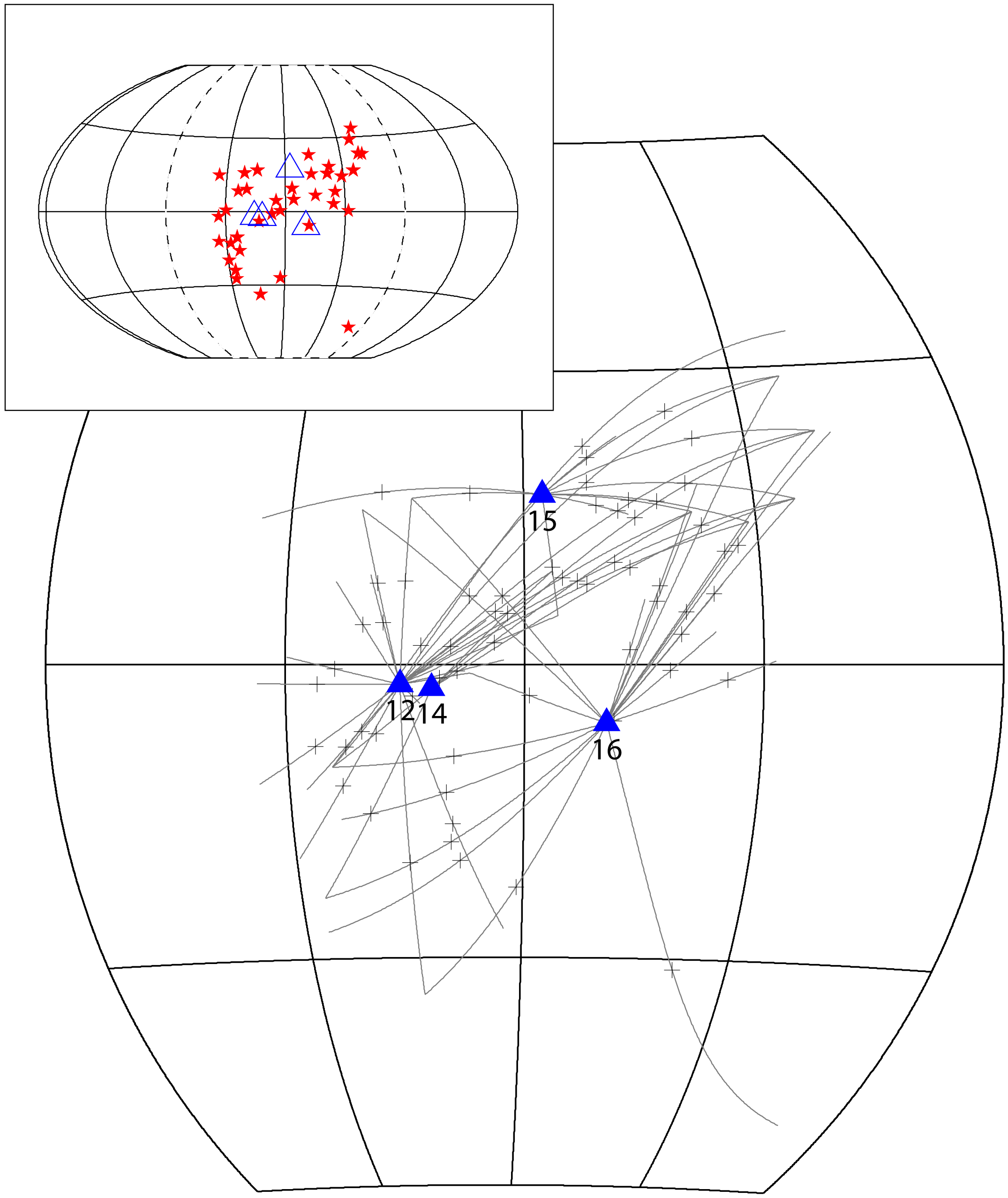

Figure S2: Map of bounce points (crosses on gray lines) from the 38 clusters (inset, red stars) for which S arrivals were selected (Table S1). The blue triangles mark the locations of the Apollo seismic stations. Grid increment is 45 degrees in both latitude and longitude.

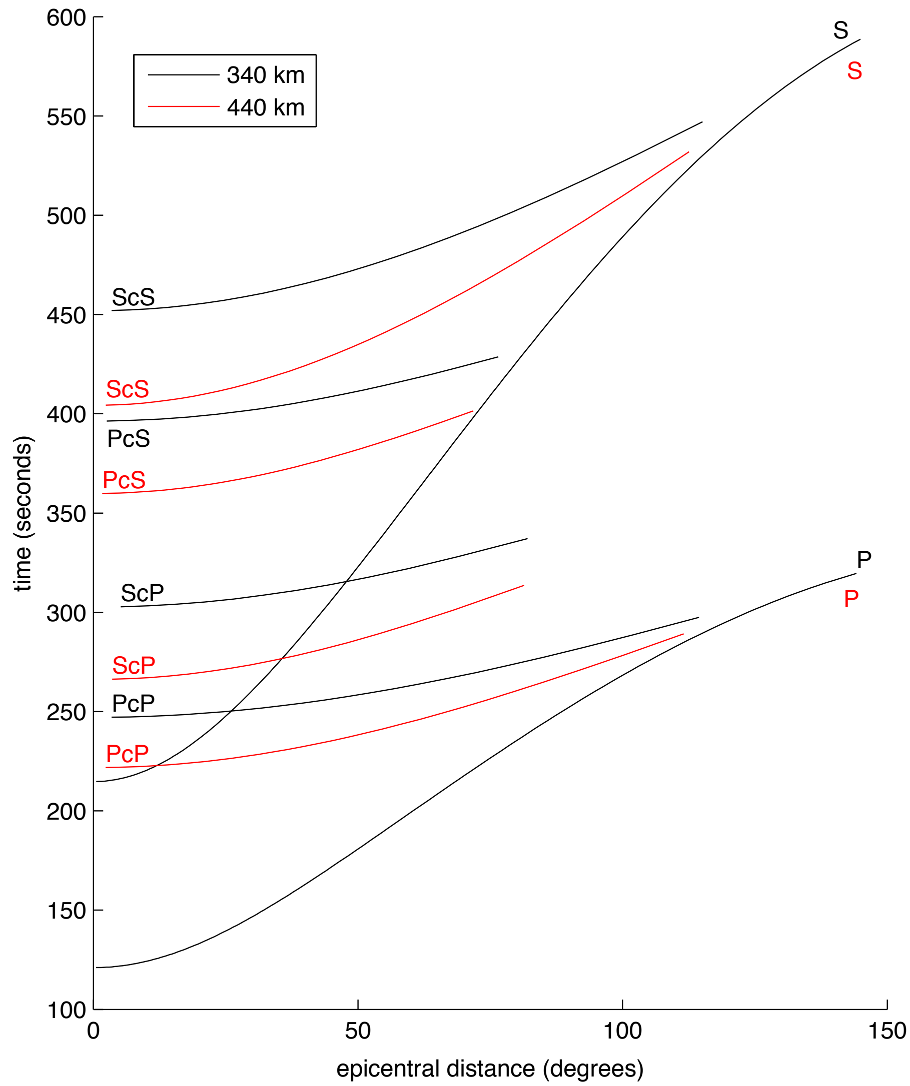

Figure S3: Travel time curves for core reflections predicted using two different core radius values: 340 km (black) and 440 km (red). Note that the timing of each phase relative to S depends on the core radius.

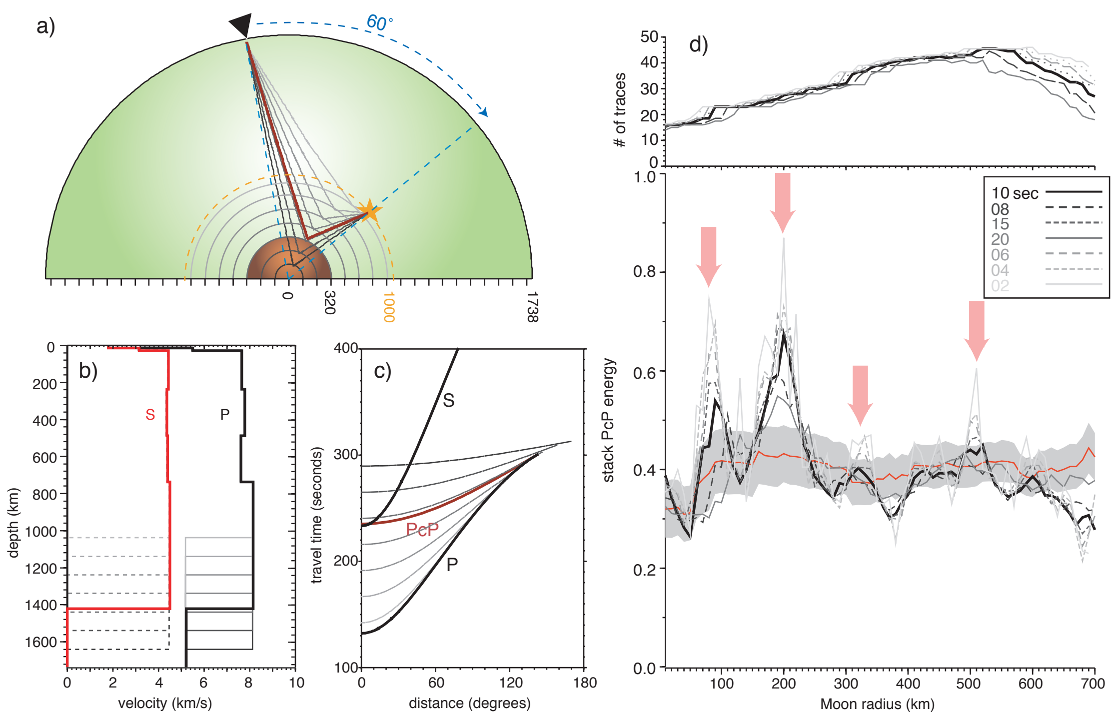

Figure S4: (a) Ray paths of PcP corresponding to varying core radii for a moonquake at lunar radius 1000 km (738 km depth). (b) Velocity model of (*S7*), extended to the CMB and illustrating the core radii shown in (a). (c) Travel time curves for PcP reflections from core radii shown in (a). (d) Results of double array stacking on the hypothetical move out of the PcP phase for core radii up to 700 km. Results are included for stacks using time window lengths ranging from 2 to 20 seconds. The red line shows the mean result of 1000 stacks of random time windows between P and S, with the grey shading showing ±1 standard deviation. Strong stack energy falling above one standard deviation is observed near 90 km, 200 km, 310 km, and 500 km radius in the Moon (red arrows).

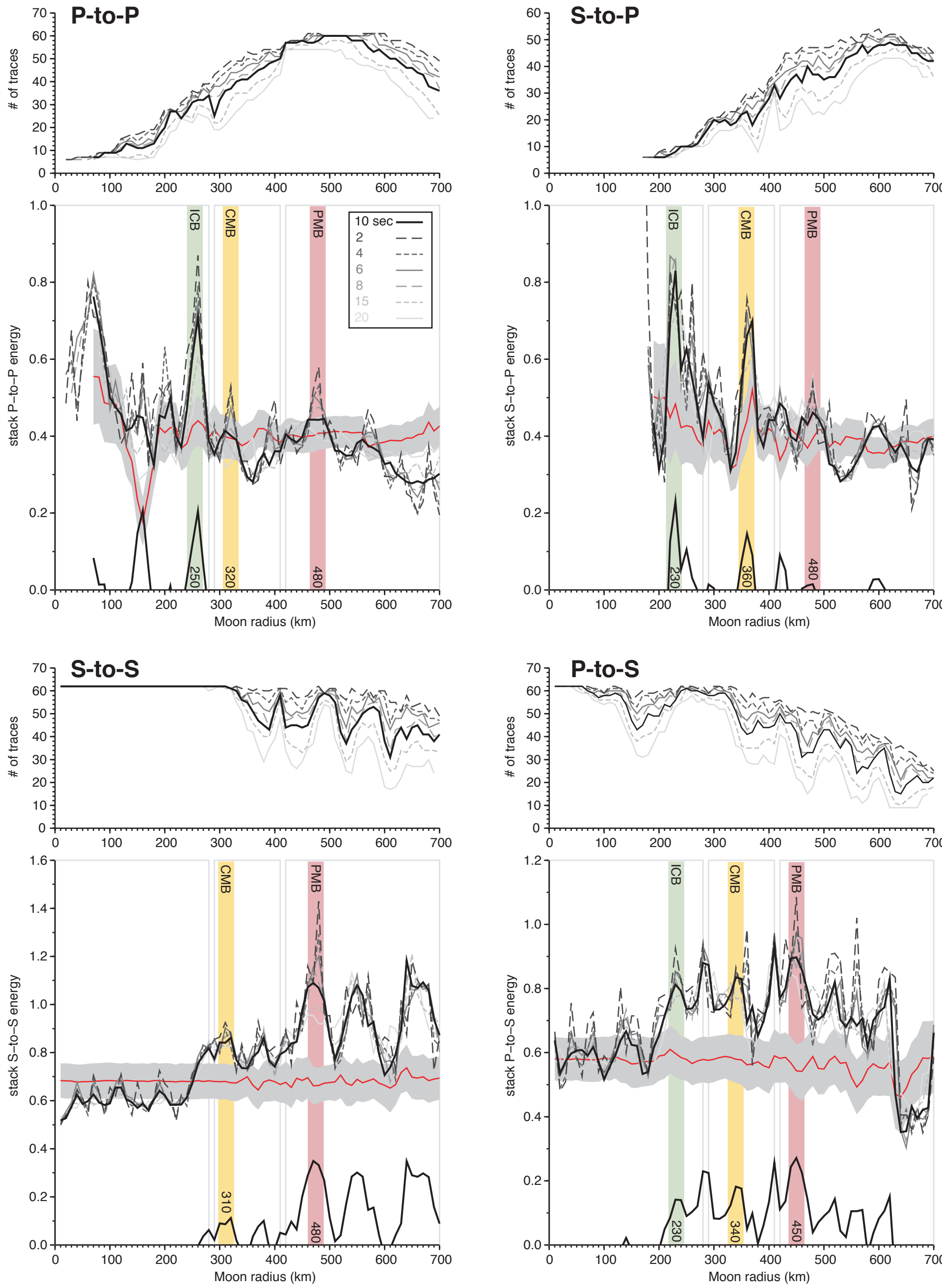

Figure S5: Same as in Fig. 2, including the results of stacking random time windows (using a 10-second window) as in Fig. S4. For clarity, the portions of the energy stack estimated from a 10-second window that fall above the mean baseline are re-plotted at the bottom of each frame.

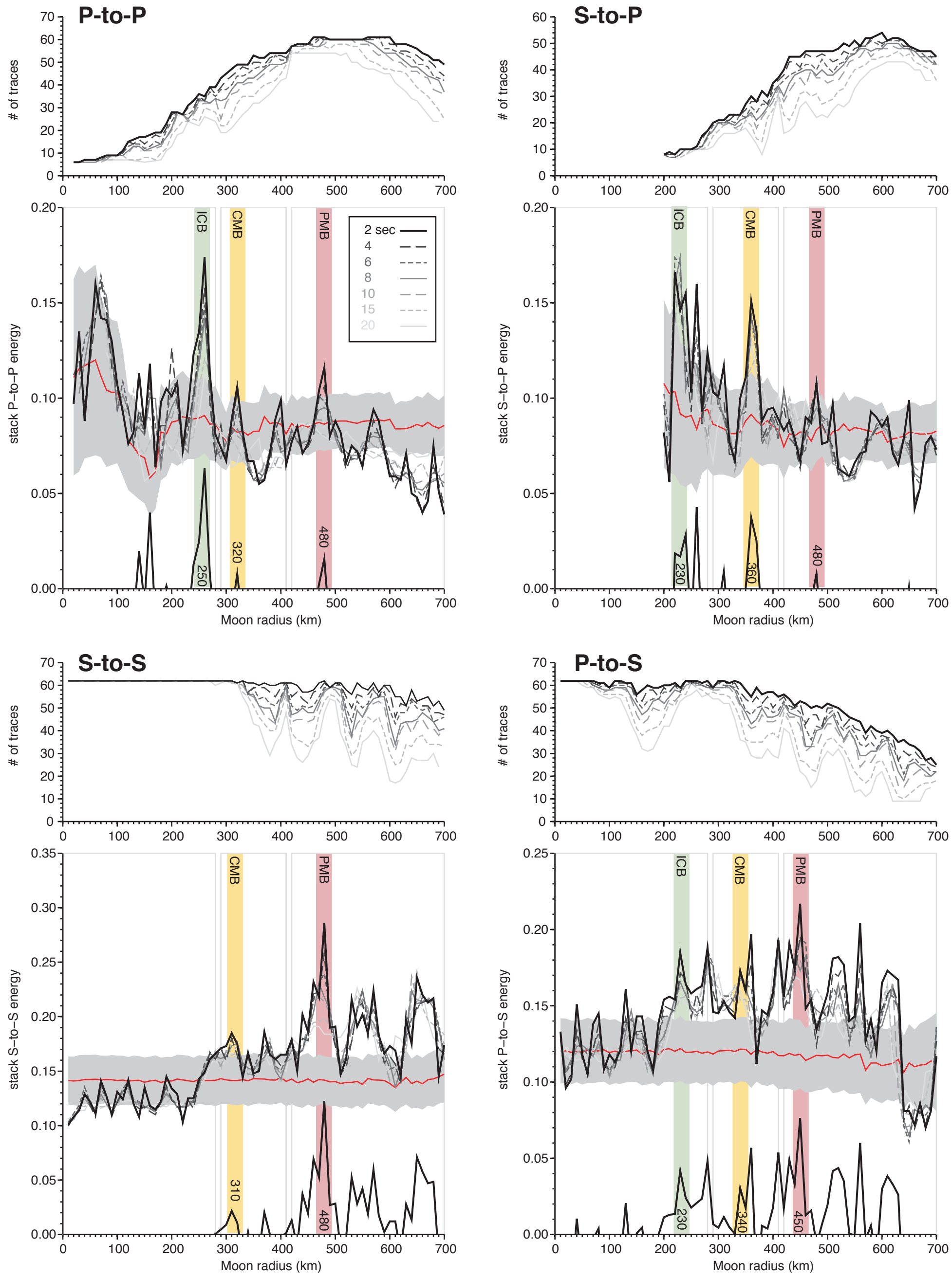

Figure S6: Same as in Fig. S5, using a 2-second window for the random trials.

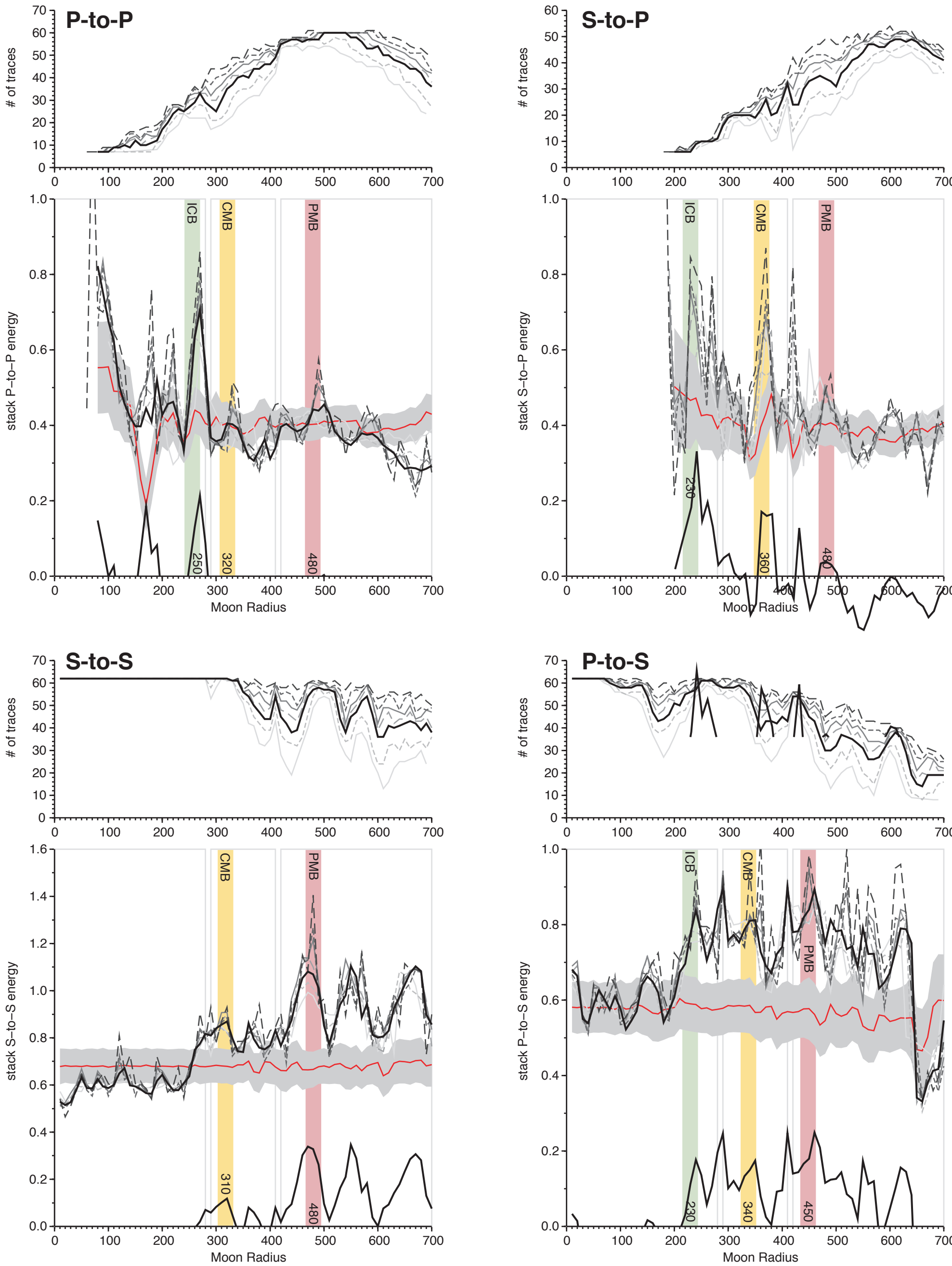

Figure S7: Stack energy plotted against core radius for a model in which the P-wave velocity in the layer above the PMB was changed from 8.5 km/s to 8.3 km/s. This lower value of compressional velocity in the deep mantle could be associated with a smaller percentage of garnet at depth. As in Figures 2 and S5, a 10-second window was used for the random trials.

Table S1: S-wave arrival picks (in seconds) given relative to an arbitrary reference time. Bold font indicates picks given a stack weighting factor of 0.5. All remaining picks received weighting factors of 0.1.

cluster	station 12	station 14	station 15	station 16
A1	226.0	**235.7**	338.9	314.6
A3	255.4			
A5	**235.1**			
A6	418.4		298.0	**371.3**
A7	410.6	**409.3**	**366.8**	**360.9**
A8				328.8
A9	244.1			
A10		289.0		297.2
A13	**260.5**			
A14	268.7			
A15	**237.3**			
A16	**271.4**		**253.2**	
A17	**238.5**		224.4	**297.3**
A18	**357.8**	337.1	270.0	281.5
A20	258.0			328.6
A21	**278.4**			
A22	**385.8**		**244.1**	**281.2**
A25	**440.4**	417.5	335.4	362.1
A26	278.2	**291.9**		
A27			**275.2**	
A30	**225.3**			
A34	**251.2**			
A35				249.0
A40	229.7			247.4
A41	**226.3**			
A42			309.8	
A44	**429.0**			
A51				290.4
A70				356.8
A82				**280.2**
A86				346.5
A97				**234.8**
A99				241.2
A201	**289.7**			
A203				323.0
A224	**328.9**			**325.0**
A241				383.5
A257			**258.5**	

Table S2: Final velocity and density structure with depth.

depth (km)	v_p (km/s)	v_s (km/s)	ρ (g/cm^3)
0.0	1.0	0.5	2.6
1.0	1.0	0.5	2.6
1.0	3.2	1.8	2.7
15.0	3.2	1.8	2.7
15.0	5.5	3.2	2.8
40.0	5.5	3.2	2.8
40.0	7.7	4.4	3.3
238.0	7.7	4.4	3.3
238.0	7.8	4.4	3.4
488.0	7.8	4.4	3.4
488.0	7.6	4.4	3.4
738.0	7.6	4.4	3.4
738.0	8.5	4.5	3.4
1257.1	8.5	4.5	3.4
1257.1	7.5	3.2	3.4
1407.1	7.5	3.2	3.4
1407.1	4.1	0.0	5.1
1497.1	4.1	0.0	5.1
1497.1	4.3	2.3	8.0
1737.1	4.3	2.3	8.0

References

S1. A. M. Dainty, M. N. Toksoz, Seismic codas on the Earth and the Moon: a comparison. *Phys. Earth Planet. Inter.* **26**, 250-260 (1981).

S2. A. M. Dainty et al., Seismic scatting and shallow structure of the Moon in Oceanus Procellarum. *The Moon* **9**, 11-29 (1974).

S3. K. D. Koper, A Fatehi, Array analysis of regional-distance P-Coda in South Asia. *Bull. Seismol. Soc. Am.* **99**, 2509-2522 (2009).

S4. K. Bataille, F. Lund, Strong scattering of short-period seismic waves by the core-mantle boundary and the P-diffracted wave. *Geophys. Res. Lett.* **23**, 2413-2416 (1996).

S5. H. S. Jarosch, The use of surface reflections in lunar seismograms. *Bull. Seismol. Soc. Am.* **67**, 1647-1659 (1977).

S6. R. L. Allen, D. W. Mills, *Signal analysis: Time, frequency, scale, and structure*. (Wiley-IEEE Press, Hoboken, NJ, 2004).

S7. P. Lognonne´, J. Gagnepain-Beyneix, H. Chenet, A new seismic model of the Moon: implications for structure, thermal evolution and formation of the Moon. *Earth Planet. Sci. Lett.* **211**, 27-44 (2003).

S8. Y. Nakamura, Farside deep moonquakes and deep interior of the Moon. *J. Geophys. Res.* **110**, E01001 (2005) doi:10.1029/2004JE002332.

S9. C. Sanloup et al., Density measurements of liquid Fe-S alloys at high-pressure. Geophys. Res. Lett. 27, 811 (2000).

S10. P. S. Balog, R. A. Secco, D. C. Rubie, D. J. Frost, Equation of state of liquid Fe-10wt% S: Implications for the metallic cores of planetary bodies. *J. Geophys. Res.* **108**, 2124 (2003) doi:10.1029/2001JB001646.

S11. M. A. Wieczorek et al., The constitution and structure of the lunar interior. *Rev. Mineral. Geochem.* **60**, 221-364 (2006).

S12. Neal, C. R.; Banerdt, W. B.; Alkalai, paper presented at the 41st Lunar and Planetary Science Conference, The Woodlands, TX, March 1-5, 2010. Sponsored by the Lunar and Planetary Institute.

S13. S. Tanaka et al., The science objectives of the SELENE-II mission as the post SELENE mission. *Adv. Space Res.* **42**, p. 394-401 (2008).

S14. L. Vinnik, H. Chenet, J. Gagnepain-Beyneix, P. Lognonne, First seismic receiver functions on the Moon. *Geophys. Res. Lett.* **28**, 3031-3034 (2001).